Featured in Physics

Single Flux Quantum-Based Digital Control of Superconducting Qubits in a Multichip Module

C.H. Liu,[1,*,‡] A. Ballard,[2] D. Olaya,[3,4] D.R. Schmidt,[3] J. Biesecker,[3] T. Lucas,[3] J. Ullom,[3,4] S. Patel,[1] O. Rafferty,[1] A. Opremcak,[1,§] K. Dodge,[2] V. Iaia,[2] T. McBroom,[2] J.L. DuBois,[5] P.F. Hopkins,[3] S.P. Benz,[3] B.L.T. Plourde,[2] and R. McDermott[1,†]

[1] *Department of Physics, University of Wisconsin-Madison, Madison, Wisconsin 53706, USA*
[2] *Department of Physics, Syracuse University, Syracuse, New York 13244, USA*
[3] *National Institute of Standards and Technology, Boulder, Colorado 80305, USA*
[4] *Department of Physics, University of Colorado, Boulder, Colorado 80305, USA*
[5] *Physics Division, Lawrence Livermore National Laboratory, Livermore, California 94550, USA*

(Received 18 January 2023; accepted 5 June 2023; published 24 July 2023)

Single flux quantum (SFQ) digital logic has been proposed for the scalable control of next-generation superconducting-qubit arrays. In the initial implementation, SFQ-based gate fidelity was limited by quasiparticle (QP) poisoning induced by the dissipative on-chip SFQ driver circuit. In this work, we introduce a multichip-module architecture to suppress phonon-mediated QP poisoning. Here, the SFQ elements and qubits are fabricated on separate chips that are joined with In-bump bonds. We use interleaved randomized benchmarking to characterize the fidelity of SFQ-based gates and we demonstrate an error per Clifford gate of 1.2(1)%, an order-of-magnitude reduction over the gate error achieved in the initial realization of SFQ-based qubit control. We use purity benchmarking to quantify the contribution of incoherent error at 0.96(2)%; we attribute this error to photon-mediated QP poisoning mediated by the resonant millimeter-wave antenna modes of the qubit and SFQ-qubit coupler. We anticipate that a straightforward redesign of the SFQ driver circuit to limit the bandwidth of the SFQ pulses will eliminate this source of infidelity, allowing SFQ-based gates with error approaching approximate known theoretical limits, of order 0.1% for resonant sequences and 0.01% for more complex pulse sequences involving variable pulse-to-pulse separation.

DOI: 10.1103/PRXQuantum.4.030310

I. INTRODUCTION

Superconducting qubits have achieved both gate [1] and measurement [2,3] fidelity at the threshold for fault-tolerant operation [4]. Recent demonstrations of quantum advantage [5] and of distance-3 and distance-5 surface codes [6–8] motivate efforts to scale to larger multiqubit arrays that are compatible with robust error correction. However, theoretical estimates suggest that a practical error-corrected quantum computer will require more than 10^6 physical qubits, for physical hardware at the current level of fidelity [4]. While it is believed that current quantum-classical interface technology can be scaled by brute force to implement systems with around 1000 physical qubits, limited by the heat load and physical footprint of the control hardware [9], no clear path is known for further scaling up. There have been serious steps to address specific obstacles to scaling, including the establishment of quantum links between separated cryogenic systems [10], the optimization of room-temperature hardware design for a more compact microwave unit [11], the integration of cryogenic CMOS-based microwave pulse generators into qubit cryostats for proximal control [12,13], the utilization of low heat-load photonic links to route control and measurement signals within the cryostat [14], and the development of compact low-heat-load microcoax cables [15]. However, an integrated systems engineering approach to scaling superconducting qubits is so far lacking.

Typically, qubit control is achieved with shaped microwave pulses derived from room-temperature

*chuanhongliu@berkeley.edu
†rfmcdermott@wisc.edu
‡Present address: Department of Physics, University of California, Berkeley, CA 94720, USA.
§Present address: Google Quantum AI, Goleta, California 93117, USA.

Published by the American Physical Society under the terms of the Creative Commons Attribution 4.0 International license. Further distribution of this work must maintain attribution to the author(s) and the published article's title, journal citation, and DOI.

digital-to-analog converters and microwave generators; the hardware overhead associated with microwave-based qubit control is one of the major obstacles to scaling to large system sizes. An alternative approach is based on single flux quantum (SFQ) digital logic [16–22]. Here, the qubit mode is irradiated with a train of quantized flux pulses, with pulse-to-pulse timing adjusted to induce a coherent rotation in the computational subspace and to minimize leakage [23]. This approach, in conjunction with digital qubit readout using the Josephson photomultiplier [3,24,25], forms the basis of a scalable quantum-classical interface for ultralarge qubit arrays [26]. An initial experiment to implement SFQ-based control of superconducting qubits has yielded a fidelity of 95% for $\pi/2$ and π rotations [27]; the gate fidelity has been limited by quasiparticle (QP) poisoning [28] associated with operation of the dissipative SFQ-pulse generator, which has been fabricated on the same chip as the qubit. In a more recent experiment, digital control of a three-dimensional (3D) transmon qubit with an error per Clifford gate of 2.1(1)% has been demonstrated using a Josephson pulse generator [29] located at the 3-K stage of the cryostat [30]. There have been separate theoretical proposals for high-fidelity SFQ-based control sequences involving variable pulse-to-pulse separation [31,32], for SFQ-based entangling gates [33], and for a scalable multiqubit architecture based on SFQ control [34]. However, a key prerequisite to the adoption of SFQ control for large-scale multiqubit arrays is the realization of high-fidelity single-qubit rotations. It is critical to investigate all the potential error channels and to understand the fundamental limits to fidelity, chief among them generation of QPs by the dissipative SFQ-pulse driver.

In this work, we adopt a multichip-module (MCM) architecture to segregate the SFQ-pulse driver and the qubit onto two separate chips. In so doing, we suppress both phonon-mediated QP poisoning and direct diffusion of QPs from the SFQ driver to the qubit. We demonstrate an order-of-magnitude reduction in SFQ-based gate infidelity, from an average error per Clifford gate of 9.1% achieved in Ref. [27] to the average error per Clifford of 1.2(1)% demonstrated in this work. We find that the infidelity is dominated by incoherent error associated with *photon*-mediated QP poisoning. We anticipate that straightforward design changes to the SFQ driver and appropriate QP mitigation on the qubit chip can lead to further reductions in gate infidelity, to the point at which we are limited by leakage to errors of order 0.1% with naive resonant control [23] and 0.01% for optimized control sequences [31,32].

This paper is organized as follows. In Sec. II, we present the quantum-classical MCM and describe basic SFQ-based single-qubit control. In Sec. III, we describe randomized benchmarking (RB) and interleaved randomized benchmarking (IRB) to characterize the fidelity of $\pi/2$, π, and average Clifford rotations and we perform detailed error budgeting of SFQ-based gates. In Sec. IV, we show that the infidelity is dominated by a subtle form of QP poisoning associated with the emission of pair-breaking photons from the SFQ driver. In Sec. V, we present simulation results that validate our model for photon-assisted QP poisoning mediated via spurious antenna modes of the qubit and SFQ-qubit coupler. Finally, in Sec. VI, we discuss straightforward modifications to the SFQ-qubit architecture to further suppress the QP-induced gate infidelity. These improvements should allow us to access gate fidelity comparable to that achieved with state-of-the-art microwave-based gates but with a compact streamlined hardware footprint for the control system.

II. QUANTUM-CLASSICAL MCM AND SFQ-BASED QUBIT CONTROL

To suppress QP poisoning, the dominant source of infidelity in previous approaches to SFQ-based qubit control [27], we segregate the qubit and SFQ elements onto two separate chips that are bump bonded with In to form the

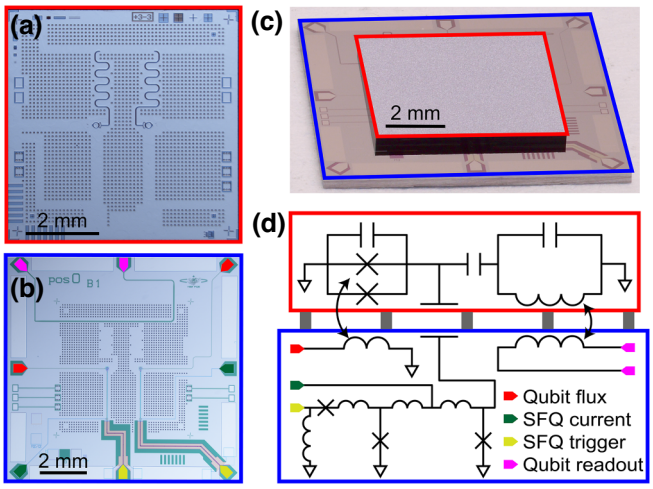

FIG. 1. The quantum-classical multichip module (MCM). (a) A micrograph of the qubit chip. Two flux-tunable transmons are fabricated on the chip, each with a local quarter-wave coplanar resonator for readout. (b) A micrograph of the SFQ driver chip. Two dc-to-SFQ converters are integrated on the chip, along with the feed line for the readout resonators and flux-bias lines for the qubits. The In bumps are visible as the regular grid pattern over the continuous ground plane. (c) A photograph showing the assembled MCM stack; the qubit chip is outlined in red and the SFQ chip is outlined in blue. (d) The circuit diagram for one qubit-SFQ pair; here, the quarter-wave readout mode is depicted using its lumped-element equivalent. In-bump bonds between the ground planes provide the only galvanic connection between the two chips; coupling between circuit elements across the chip-to-chip gap is achieved either capacitively or inductively. The colors used in the legend to identify specific circuit elements are matched to the false coloring of the bond pads in the image of (b).

MCM stack shown in Fig. 1. The qubit chip shown in Fig. 1(a) incorporates two flux-tunable transmon qubits, each with its own local quarter-wave resonators for state measurement. The SFQ driver chip shown in Fig. 1(b) incorporates two dc-to-SFQ converters along with all control and readout lines for the qubits. The two chips are bonded by In bumps to form the MCM via the technique described in Appendix A 3 [see Fig. 1(c)]. The MCM architecture suppresses QP poisoning of the qubit in two ways. First, the direct diffusion of QPs from the SFQ driver to the qubit is not possible, as the two elements reside on separate chips that are separated by low-gap In-bump bonds: QPs that relax to the In gap edge will be unable to enter the Nb ground plane of the quantum chip [35]. Similarly, pair-breaking phonons that propagate to the In-bump bonds are expected to scatter to the In gap edge through electron-phonon interaction, so that phonons will have insufficient energy to enter the Nb ground plane of the qubit chip; acoustic mismatch across the bump bonds will further inhibit phonon propagation from chip to chip. In Fig. 1(d), we show a simplified circuit diagram for one qubit-SFQ pair, with the qubit readout resonator depicted as its lumped-element-equivalent tank circuit. Each qubit-SFQ pair involves one flux bias line for the qubit, one current bias line for the SFQ driver, and one microwave drive line to trigger SFQ pulses. The qubit readout line is shared between the two qubit-SFQ pairs. Details of the experimental setup are given in Appendix B.

The quantum-classical MCM is characterized in a closed-cycle dilution refrigerator at a base temperature of 20 mK. Preliminary optimization of SFQ-based qubit rotations is described in Fig. 2. To generate a well-controlled SFQ pulse train from the driver circuit, we provide dc bias to the SFQ current port and we apply a shaped microwave pulse to the SFQ trigger port. The bias current is adjusted to be slightly less than the critical current of the device and the frequency of the microwave trigger pulse is adjusted to the desired frequency f_{SFQ} of the SFQ pulse train. To avoid direct drive of the qubit via crosstalk from the SFQ trigger line, we generate an SFQ pulse train at a subharmonic of the fundamental qubit frequency f_{01}. In the experiments described here, we drive the qubit at the frequency $f_{\mathrm{SFQ}} = f_{01}/4$. With the SFQ trigger tone applied, we sweep the current bias I_b of the SFQ-pulse driver to determine an operating regime where the induced qubit Rabi frequency is insensitive to SFQ driver bias; the results are shown in Fig. 2(a). Over the optimal range of SFQ driver operation, we find a weak dependence of Rabi frequency on I_b; we discuss possible explanations for this dependence in Appendix C. In Fig. 2(b), we show the results of a Rabi chevron experiment used to fine tune the SFQ drive frequency. Finally, we perform the generalized Rabi experiment described in Fig. 2(c) in order to identify the duration and relative timing of SFQ pulse trains needed to execute qubit rotations about arbitrary control vectors oriented in the equatorial plane of the Bloch sphere. The symbol ϕ in Fig. 2(c) refers to the phase associated with the relative timing of the initial $X/2$ pulse train and the subsequent pulse train R_{SFQ}. By controlling the phase relationship between the two pulse trains, it is possible to realize full orthogonal control of the qubit.

III. BENCHMARKING OF SFQ GATES

After demonstrating basic qubit control with SFQ pulse trains, we characterize the fidelity of SFQ-based gates. It is critical to find the set of parameters in the multidimensional SFQ operation space to optimize the gate fidelity. In this work, the SFQ control parameters include the bias current I_b, the trigger frequency f_{SFQ}, the phase difference between orthogonal rotations, the trigger amplitude,

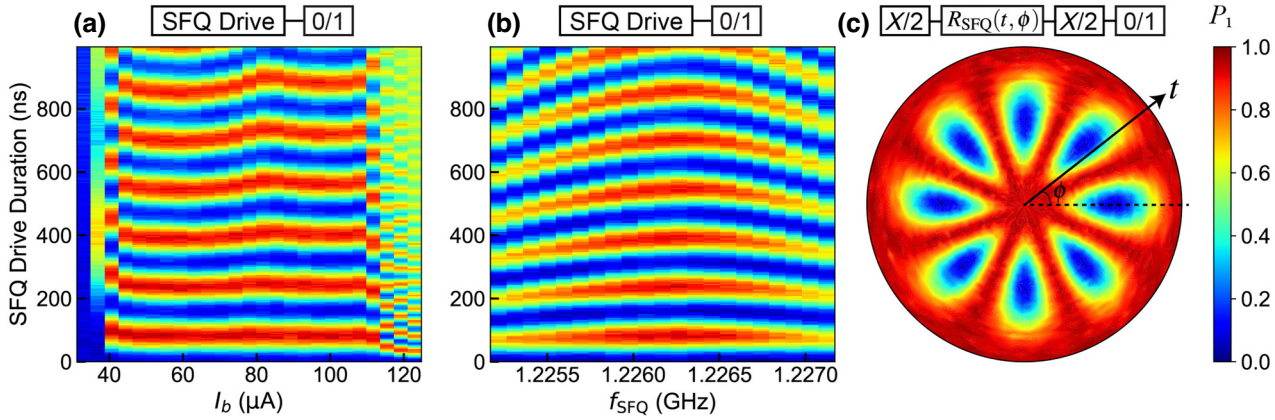

FIG. 2. SFQ-based qubit operation at the subharmonic drive frequency $f_{01}/4$. (a) Rabi oscillations as a function of the current bias I_b of the SFQ driver. (b) The Rabi chevron experiment at variable drive frequency in the vicinity of $f_{01}/4$. (c) The generalized Rabi scan at $f_{01}/4$, with variable time t and phase ϕ for the Rabi drive; the inset illustrates the relationship between the phase ϕ and the relative timing of the pulse trains used to implement the $X/2$ and R_{SFQ} rotations.

and related mixer-calibration parameters of the trigger signal. Here, we follow a two-step optimization procedure involving error amplification to tune up individual gates followed by global optimization using randomized benchmarking (RB) [37,38]. Initially, we find the best operating parameters for each individual gate. We construct equivalent identity and π-pulse sequences by concatenating many instances of the individual gate, e.g., $S_1 = X^{30}$, and $S_2 = X^{31}$. We measure the difference of $|1\rangle$-state occupation following application of the two sequences $P_1(S_2) - P_1(S_1)$ while sweeping the SFQ drive parameters and we adjust the parameters to maximize the sequence contrast. We find that the optimal parameters for the SFQ driver are not exactly the same across all SFQ-based gates. For global optimization of SFQ-based gates, including optimization of the time delay associated with orthogonal rotations on the Bloch sphere, we maximize the RB sequence fidelity following the ORBIT method developed in Ref. [39].

Following optimization of the SFQ gate parameters, we use the technique of interleaved RB to access the gate fidelity independent of state-preparation-and-measurement error [40]. The set of single-qubit Clifford gates used in the reference RB sequence is listed in Table II. Here, we evaluate the fidelity of the set of gates $\{X, Y, \pm X/2, \pm Y/2\}$. In Fig. 3, we present RB and interleaved-RB data taken across 6 h, highlighting the temporal stability of SFQ-based single-qubit control. A fit to the reference curve yields the average Clifford-gate fidelity $F_{\text{Cliff}} = 0.988(1)$. From the interleaved-RB scans, we extract the gate fidelities shown in the inset of Fig. 3(c). As a check, we calculate the fidelity of an average Clifford gate from the extracted fidelities of the six interleaved gates. The appropriate weighted sum over the interleaved gates fidelities yields an average Clifford-gate fidelity of 0.988(3), consistent with the measured RB value $\mathcal{F}_{\text{Cliff}}$.

The measured error associated with SFQ-based control shows a one-order-of-magnitude reduction compared to the first-generation result of [27]. Accurate understanding of the source of the error is critical to further optimization of SFQ-based gates. As a starting point, we need to distinguish between coherent and incoherent error. The former involves pulse sequence miscalibration, while the latter is due to qubit dissipation via uncontrolled coupling to the environment. Here, we use purity benchmarking [41] to extract the incoherent contribution to the error. The gate sequence is shown in Fig. 4(a). We apply a random sequence of m Clifford gates followed by quantum state tomography to determine the purity of the qubit state. The decomposition of the Clifford gates used in purity benchmarking is the same as that shown in Table II. A fit to the purity curve yields an incoherent error for the average Clifford gate of $r_{\text{Cliff, inc}} = 0.96(2) \times 10^{-2}$. From RB, we find an error per Clifford gate of $r_{\text{Cliff}} = 1 - \mathcal{F}_{\text{Cliff}} = 1.2(1) \times 10^{-2}$. We see that 80% of the error is due to incoherent processes. In Fig. 4(b), we plot the error of

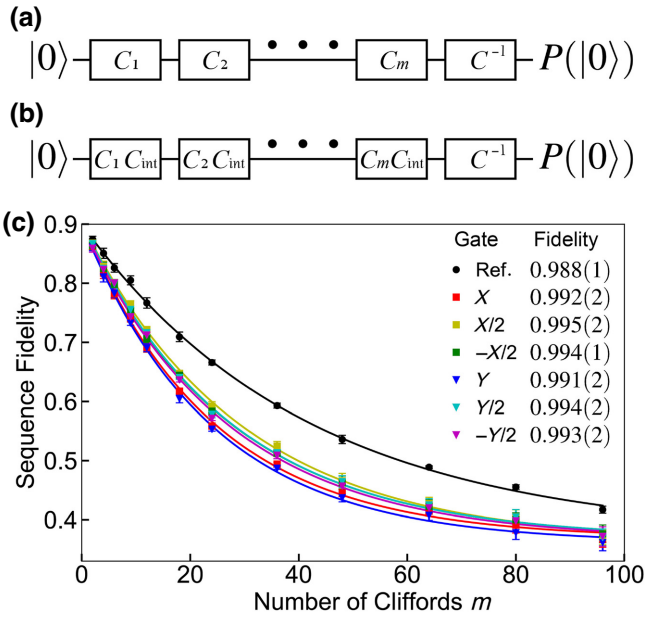

FIG. 3. (a),(b) Randomized benchmarking (RB) of SFQ-based gates with the drive at frequency $f_{01}/4$ = 1.2264 GHz: pulse sequences for (a) reference and (b) interleaved RB. (c) Depolarizing curves for the reference RB sequence and six interleaved-RB sequences. Each data point is the average of 150 random sequences across 6 h. The inset shows the fidelities of the average Clifford gate [36] and the six interleaved gates.

the six interleaved gates characterized previously and of the average Clifford gate versus gate time. The average Clifford-gate time is 90.4 ns, 2.26 times that of the $\pi/2$ gate. We see that gate error increases with gate duration. The dashed blue line in Fig. 4(b) shows the baseline incoherent error per gate $t_{\text{gate}}/T_{\text{error}}$ [42], where t_{gate} is the gate length and where $1/T_{\text{error}} = 1/3(1/T_{2,\text{white}} + 1/T_1)$ is calculated from the qubit coherence times (for details, see Table I in Appendix D) measured using conventional microwave-based sequences with the SFQ driver turned off [43]. Comparing this baseline error to the measured incoherent error for the average Clifford gate, we see that operation of the SFQ-pulse driver induces additional incoherent error around 2.6 times that of the baseline. In Sec. IV, we show that photon-assisted QP poisoning is the source of the additional incoherent error.

IV. DYNAMICS OF QP POISONING

Nonequilibrium QPs are a dominant decoherence source for superconducting quantum devices [44–48] and suppression of QP poisoning associated with the dissipative SFQ-pulse driver is the primary reason for adopting the MCM architecture described here. The analysis above indicates that SFQ gate infidelity is dominated by incoherent error and that operation of the SFQ-pulse driver leads

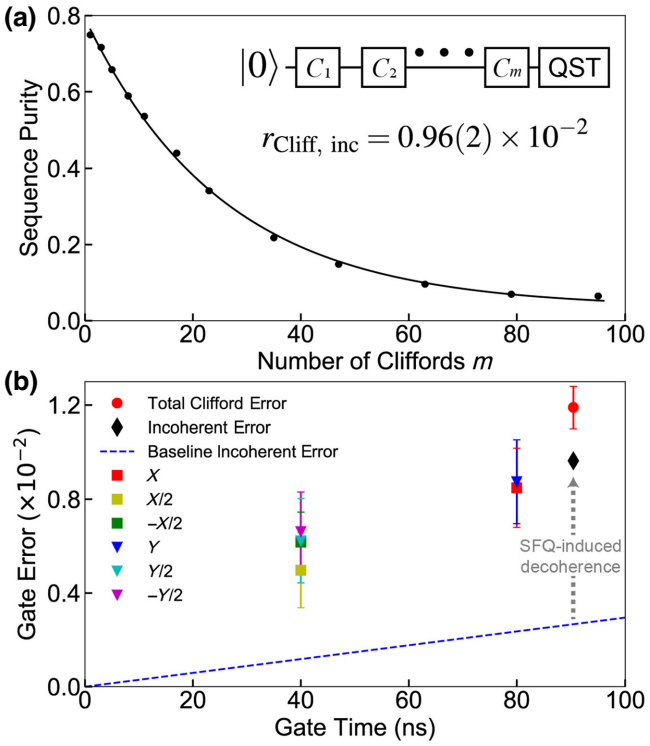

FIG. 4. The characterization of incoherent error. (a) Purity benchmarking of SFQ-based gates at pulse frequency $f_{01}/4 = 1.2264$ GHz. The inset shows the gate sequence for purity benchmarking. Here, quantum state tomography is applied at the end of the m randomized Cliffords. The incoherent error per Clifford, $r_{\text{Cliff, inc}}$, is extracted from the purity of the final state. (b) The gate error derived from the RB measurements of Fig. 3(c) versus the gate duration. For the average Clifford gate (black diamond), incoherent errors constitute 80% of the total error (red circle). The blue dashed line shows the baseline incoherent error of 0.27×10^{-2} for the average Clifford gate extracted from the coherence times of the qubit measured with microwave-based gates in the absence of SFQ operation.

to significant suppression of qubit coherence. QP poisoning remains the most likely mechanism for suppression of qubit coherence. To quantify the generation of QPs at the qubit chip from operation of the SFQ-pulse driver, we perform microwave-based inversion-recovery experiments following application of an off-resonant SFQ drive and we fit the recovery signal to the form [49,50]

$$P_1(t) = e^{\langle n_{\text{qp}}\rangle\left(\exp(-t/T_{1,\text{qp}})-1\right)-t/T_{1,R}}, \tag{1}$$

where $P_1(t)$ is the $|1\rangle$-state occupation of the qubit, $\langle n_{\text{qp}}\rangle$ is the mean number of QPs coupled to the qubit, $T_{1,\text{qp}}$ is the qubit energy relaxation time per QP, and $T_{1,R}$ is the energy relaxation time due to remaining relaxation channels. The above relation comes from averaging the qubit free-induction decay signal over an ensemble of quasiparticles coupled to the qubit junction that follows a Poisson distribution with mean number $\langle n_{\text{qp}}\rangle$. In Fig. 5(a), we plot inversion-recovery signals measured with (red points) and without (blue points) application of a 7-μs off-resonant SFQ poisoning pulse prior to the measurement. The solid traces are fits to the data from Eq. (1) to extract $\langle n_{\text{qp}}\rangle$. In a separate experiment, we vary the poisoning pulse length prior to the T_1 measurement. Fits to the inversion-recovery scans yield $T_{1,\text{qp}} = 6.8(6)$ μs and $T_{1,R} = 26(1)$ μs; in Fig. 5(b), we plot $\langle n_{\text{qp}}\rangle$ as a function of the poisoning length. The data are well described by a model where the rate of QP removal is linear in QP density, as expected for both diffusion of QPs from the junction and QP trapping at defect sites. We express the time-dependent QP population as follows [51,52]:

$$\langle n_{\text{qp}}(t)\rangle = \frac{G}{s}(1 - e^{-st}), \tag{2}$$

where G is the QP generation rate and s is the QP removal rate. Removal can be due to several different physical processes: quasiparticle recombination, out-diffusion from the junction area, or trapping at defect sites. Here, we use a simplified linear decay model where all of these processes are folded into the single rate s; we find that this model provides a reasonable description of the quasiparticle dynamics in our experiment. We find $G = 0.14(2)$ μs^{-1} and $s^{-1} = 2.8(4)$ μs. The generation rate corresponds to $3.7(5) \times 10^{-5}$ QPs coupled to the qubit per phase slip of the SFQ driver, a factor-of-43 improvement compared to the QP poisoning seen in the first-generation SFQ control experiments of [27].

Our next task is to understand the physical mechanism for QP poisoning in the MCM architecture. There are two possibilities. In one scenario, QP poisoning is mediated by pair-breaking phonons that propagate from the classical chip to the quantum chip [53], despite the presence of the low-gap In bumps that are expected to promote phonon relaxation below the gap edge of the Nb ground plane of the quantum chip. Alternatively, QP poisoning could be dominated by pair-breaking *photons* associated with the ultrahigh-bandwidth SFQ pulses. It is known that qubit structures are efficient absorbers of pair-breaking radiation in the millimeter-wave range [54,55]; for picosecond SFQ pulses with a bandwidth of the order of hundreds of gigahertz, the electromagnetic transient could lead to emission of pair-breaking photons that are then absorbed at the qubit junction. We expect to be able to distinguish these two processes by examining the temporal dynamics of QP poisoning in our experiment: while the photon-assisted QP poisoning mechanism will lead to immediate suppression of qubit coherence, the phonon mechanism will involve a time delay of the order of tens of microseconds between application of the SFQ pulse and the onset of enhanced QP relaxation associated with the propagation of phonons from the SFQ driver to the qubit [56].

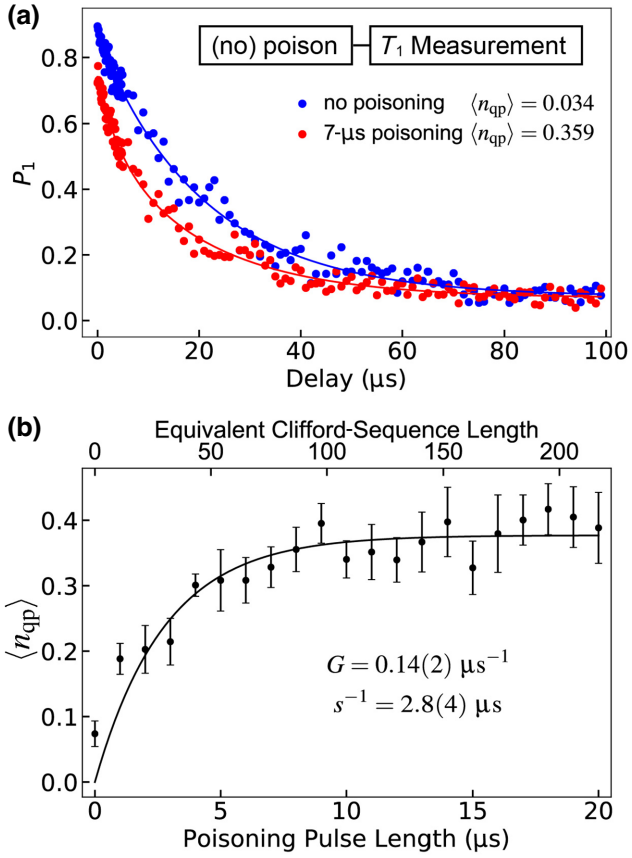

FIG. 5. QP poisoning induced by operation of the SFQ-pulse driver. (a) Microwave-based energy relaxation curves of the qubit with and without prior application of an off-resonant SFQ pulse train at $f_{SFQ} = 1.21$ GHz. The mean number $\langle n_{qp}\rangle$ of QPs coupled to the qubit is extracted from a fit of Eq. (1) to the data. (b) $\langle n_{qp}\rangle$ versus the SFQ poisoning pulse length. Each point is extracted from eight T_1 traces of the type shown in (a).

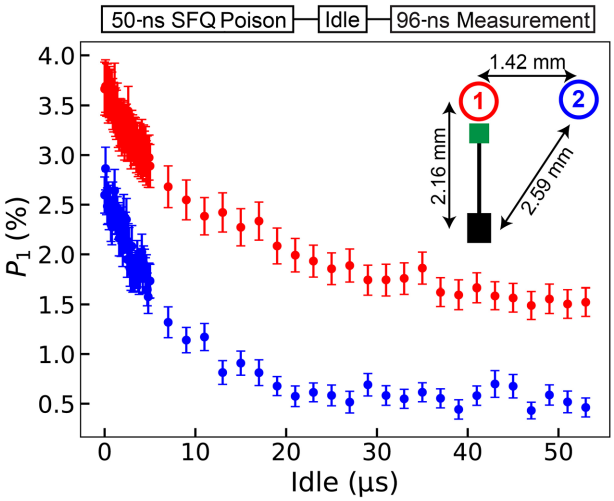

FIG. 6. The dynamics of QP poisoning from the SFQ-pulse driver. A variable idle time follows application of a brief SFQ poisoning pulse; subsequent fast-qubit measurement is used to extract the qubit $|1\rangle$-state occupation P_1. The inset shows the relative positions of Q_1 (red), Q_2 (blue), the dc-to-SFQ converter (black rectangle), and the SFQ-qubit coupling capacitor (green square). For both qubits, P_1 decays monotonically with the idle time. We observe no time lag between application of the poisoning pulse and the peaking of enhanced excess P_1, indicating that poisoning is mediated by pair-breaking photons, as opposed to pair-breaking phonons.

We probe the dynamics of QP poisoning in the MCM by applying a short 50-ns burst of off-resonant SFQ pulses, using the two qubits on the MCM as QP sensors. We increment the relative delay between application of the poisoning pulse and qubit measurement; in order to access short time scales, we use a fast-qubit measurement with duration of 96 ns. The geometry of the experiment is shown in the inset of Fig. 6. We find that the effect of QP poisoning is to increase P_1, where the baseline levels of qubits 1 and 2 are 1.6% and 0.5%, respectively. This fact alone argues in favor of the photon-mediated mechanism, which drives upward qubit transitions far more efficiently than diffusion across the qubit junction of QPs that are resident in the junction leads [57]. We probe qubit population P_1 as a function of idle time following the poisoning pulse; the results are shown in Fig. 6. We find a monotonic decrease in excess P_1 toward the baseline value following application of the poisoning pulse. In a similar experiment involving the injection of pair-breaking phonons into the qubit substrate, Iaia *et al.* have observed a QP-induced enhancement of the qubit relaxation rate that peaks at a time of approximately 30 μs following application of the poisoning pulse, consistent with diffusive propagation of phonons from the injector junction to the qubit over the approximately 4-mm separation between the elements [56]. We take the much faster response of the qubit to the poisoning pulse observed in our experiments as further evidence that coupling of the SFQ driver to the qubit is mediated by photons as opposed to phonons.

V. ANTENNA COUPLING OF THE SFQ TRANSIENT TO THE QUBIT

It has recently been shown that absorption of pair-breaking photons is a dominant source of QP poisoning in Josephson devices [55,57–59]. For typical geometries, the superconducting-qubit structure forms a resonant antenna that provides an efficient power match from free space to the high-impedance Josephson junction at millimeter-wave frequencies [54]. Due to its short temporal duration of the order of picoseconds, the bandwidth of a single SFQ pulse is of the order of hundreds of gigahertz, sufficient to excite the millimeter-wave antenna mode of the qubit and generate QPs. In Fig. 7, we consider the antenna modes of the qubit and SFQ-coupler structures used in our experiments. The experimental geometry is shown in

Figs. 7(a) and 7(b); here, Nb metallization on the quantum and classical chips is shown in gray and the white regions indicate where the Nb has been removed. The circular qubit and the SFQ-qubit capacitive coupler both act as resonant aperture antennas with efficient coupling to free space at millimeter-wave frequencies. Following the modeling described in Ref. [54], we plot the free-space coupling efficiency e_c of the bare-qubit-antenna mode as the black curve in Fig. 7(c). The structure shows a clear resonance at 240 GHz, corresponding to a match between the qubit perimeter and one full wavelength of the radiated field; higher-frequency peaks correspond to harmonics of this fundamental mode.

In the same figure, we plot the coupling efficiency of the qubit (red curve) and the SFQ coupler (blue curve) calculated for the full MCM structure. Both modes display a complicated frequency-dependent coupling efficiency with peaks in the resonant response around 300 GHz. The presence of a proximal ground plane in the second chip of the MCM modifies the coupling of the qubit to free space. We find that incorporation of the qubit into the MCM structure shifts the bare-qubit-antenna resonance to higher frequency. This shift is qualitatively compatible with inductive screening by the ground plane of the classical chip, since image currents induced in the continuous ground plane of the second chip will suppress the electric dipole moment of the qubit and reduce the coupling to free space [58]. Similarity in the coupling efficiency of the qubit and SFQ coupler could be due to loading of both modes by the etched cavity in the ground plane of the SFQ driver chip (see Appendix A.3). Detailed modeling of the radiative coupling of qubits in various MCM architectures is the subject of ongoing research.

After verifying that the SFQ-qubit pair can be considered as a coupled antenna system, we show that the picosecond-scale SFQ pulse indeed leads to emission of photons with energy sufficient to break Cooper pairs (for a detailed discussion, see Appendix I).

From our analysis of QP poisoning presented in Fig. 5, a single SFQ pulse delivered to the qubit generates 1.1×10^{-4} QP at the qubit junction. We can ask the question: if all the energy that goes into QP generation is derived from SFQ-qubit antenna coupling, what is the efficiency of energy transfer from the driver to the qubit? We define an energy-conversion factor α as follows:

$$\alpha E_{\mathrm{SFQ}} = 1.1 \times 10^{-4} \times E_{\mathrm{qp}}, \tag{3}$$

where E_{SFQ} is the available energy from one SFQ pulse and E_{qp} is the energy of one QP. We take the available energy per SFQ pulse to be equal to the phase slip energy and, for simplicity, we assume that the generated QPs are concentrated at the gap edge of Al. We find

$$E_{\mathrm{SFQ}} = I_c \Phi_0, \tag{4}$$

$$E_{\mathrm{qp}} = h \times 50\ \mathrm{GHz}, \tag{5}$$

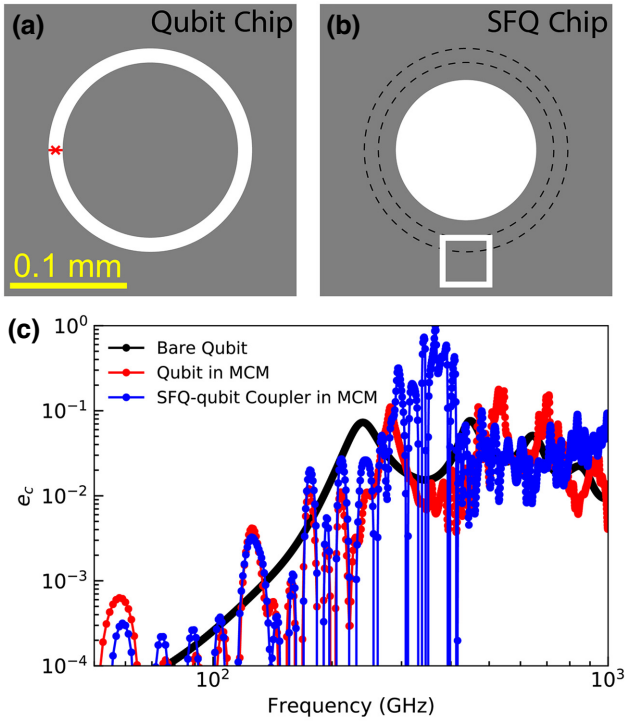

FIG. 7. Antenna modeling of the qubit and the SFQ-qubit coupler. Schematics of (a) the qubit and (b) the region opposite the qubit on the classical SFQ driver chip. Here, gray represents Nb metallization on the two chips; in the white regions, the Nb has been etched away. The qubit island is a circular pad with radius 75 μm. embedded in a circular ground-plane cavity with radius 87 μm. The Nb has been removed in a circular region on the classical chip directly opposite the qubit island in order to reduce the capacitance between the qubit and the ground plane of the classical chip. In (a), the position of the qubit junction is indicated by the red cross. In (b), the concentric black dashed lines indicate the position of the gap between the qubit island and ground plane relative to structures on the SFQ driver chip. The patch capacitor that couples SFQ pulses to the qubit is shown at the bottom; the capacitor is realized as a square electrode with dimension 35 μm × 35 μm. embedded in a cavity in the ground plane with dimension 45 μm × 45 μm. The SFQ-qubit coupler is fed from below the image by a microstrip line from the classical SFQ driver circuit (not shown). (c) The numerically calculated free-space coupling efficiency e_c of the antenna modes of the qubit and of the SFQ-qubit coupler [54]. The black curve represents e_c of the qubit with the SFQ chip removed; the dominant feature at 240 GHz corresponds to the fundamental full-wave resonance of the aperture antenna formed by the qubit island embedded in the ground plane. The red and blue traces are simulation results for e_c of the qubit and SFQ-coupler modes calculated in the full MCM architecture.

where $I_c \sim 100$ μA is the critical current of the output junction of the SFQ driver. Solving the above equations, we find an experimental energy-conversion efficiency $\alpha_{\rm exp} = 1.8 \times 10^{-8}$.

We can compare the experimentally extracted α with the result derived from time-domain modeling of the coupled antenna system. We take $R_{\rm SFQ} = 1\ \Omega$ as the source impedance associated with the SFQ-qubit coupler and we model the SFQ transient as a Gaussian pulse with width $\sigma = 2.5$ ps, derived from WRspice [60] simulation of our dc-to-SFQ converter. As shown in Fig. 8(a), the SFQ pulse applied to the coupler (blue) induces an oscillatory voltage response at the qubit junction port (red, scaled by a factor 50), with a dominant frequency set by the product of the energy spectral density of the SFQ pulse and the photon-coupling efficiency of the coupler-qubit system. In Fig. 8(b), we show in red the energy spectral density of the response signal at the qubit port $|\widetilde{V}_{\rm qb}|^2/R_{\rm qb}$; here, $\widetilde{V}_{\rm qb}$ is the Fourier transform of the voltage induced at the qubit port and $R_{\rm qb} = 8.0\ {\rm k}\Omega$ is the normal-state resistance of the junction. As in Ref. [55], we define the photon-coupling efficiency η as

$$\eta(f) = e_{c,{\rm qb}}\, e_{c,{\rm coupler}}, \tag{6}$$

where f is frequency and $e_{c,{\rm qb}}$ ($e_{c,{\rm coupler}}$) is the coupling efficiency of the qubit (coupler) calculated in Fig. 7(c). In Fig. 8(b), we plot in blue the available energy spectral density from the SFQ pulse $|\widetilde{V}_{\rm SFQ}|^2/R_{\rm SFQ}$ scaled by the coupling efficiency η. The close agreement with the spectrum calculated from the voltage transient at the qubit junction suggests that transport of pair-breaking energy between the SFQ coupler and the qubit is dominated by direct antenna coupling between the structures.

From our modeling, we calculate the total energy dissipated at the qubit port for photons with a frequency above 100 GHz and we find a simulated energy-conversion factor $\alpha_{\rm sim}(\sigma = 2.5\ {\rm ps}) = 3.8 \times 10^{-8}$, in reasonable agreement with the experimental value $\alpha_{\rm exp} = 1.8 \times 10^{-8}$. For the sake of completeness, we also simulate antenna coupling to the qubit of SFQ pulses with varying widths. For SFQ-pulse widths $\sigma = 0.5, 1, 2$, and 5 ps, we find energy-conversion efficiency $\alpha_{\rm sim} = 1.3 \times 10^{-5}, 1.3 \times 10^{-6}, 9.7 \times 10^{-8}$, and 1.0×10^{-12}, respectively. It is clear that broader SFQ pulses, for which the energy is compressed into a narrower spectral band, lead to a suppression of antenna-mediated QP poisoning at the qubit. As the typical qubit oscillation period of approximately 200 ps is orders of magnitude longer than typical SFQ-pulse widths, a straightforward redesign of the SFQ driver to suppress the spectral weight of the SFQ transient above 100 GHz provides an obvious path to eliminating photon-mediated QP poisoning. Deviation of the SFQ pulse from the ideal delta-function will cause misrotation of the qubit state vector on the Bloch sphere [30]; however, this is a coherent error that is readily addressed by appropriate gate calibration.

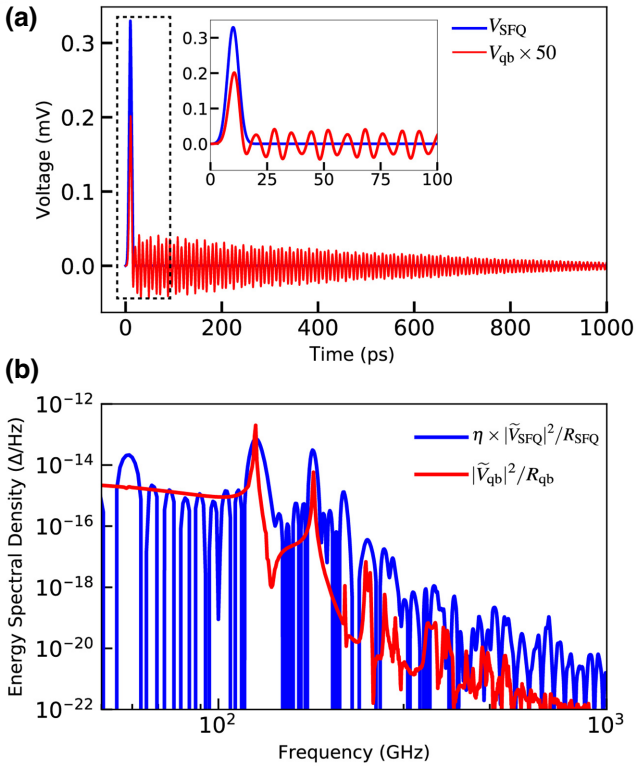

FIG. 8. The temporal response of the qubit antenna mode to a single SFQ pulse. (a) The SFQ pulse and induced transient at the qubit. A single SFQ pulse $V_{\rm SFQ}$ with $\sigma = 2.5$ ps is delivered from the SFQ-qubit coupler (blue trace). Antenna coupling between the SFQ-qubit coupler and the qubit results in an induced voltage $V_{\rm qb}$ at the qubit port (red trace; voltage scaled by a factor of 50 for clarity). (b) The energy spectral density of the qubit response expressed in units of $\Delta/{\rm Hz}$, where $\Delta = E_{\rm qp} = h \times 50$ GHz. The red trace is the energy spectral density calculated from the qubit transient in (a); here, $\widetilde{V}_{\rm qb}$ is the Fourier transform of the induced voltage at the qubit and $R_{\rm qb}$ is the normal-state resistance of the qubit junction. The blue trace shows the product of the photon-coupling efficiency η based on the frequency-domain antenna modeling and the energy spectral density of the SFQ pulse. The dominant Fourier component in the qubit response matches the product of the energy spectral density of the SFQ pulse and the photon-coupling efficiency of the coupler-qubit system.

VI. CONCLUSIONS

In this work, we advance the state of the art for SFQ-based digital control of superconducting qubits. By segregating qubits and classical control elements on separate chips in an MCM architecture, we suppress phonon-mediated QP poisoning and achieve an error per Clifford

gate of 1.2(1)%. This gate infidelity represents a one-order-of-magnitude reduction compared to the first demonstration of SFQ-based qubit control [27] and a factor-of-2 reduction in the infidelity achieved in recent work involving a 3D transmon controlled by a Josephson pulse generator located at the 3 K stage of the cryostat [30]. We find that the residual gate infidelity is dominated by photon-assisted QP poisoning mediated via spurious millimeter-wave antenna modes of the qubit and SFQ-qubit coupler. To suppress QP generation at the qubit from the high-bandwidth SFQ pulse, we suggest a modest redesign of the SFQ driver circuit to yield SFQ pulses with broader characteristic temporal width, corresponding to a narrower pulse bandwidth in the frequency domain. Such a redesign will concentrate the power emitted by the SFQ driver below the aluminum gap edge, so that QP generation is not possible. The qubit and the SFQ-qubit coupler could also be modified to suppress their antenna coupling to free space at frequencies just above the aluminum gap [54,55,58]. To protect the qubit from any residual nonequilibrium QPs, appropriate superconductor-gap engineering [35,61–64] could be harnessed to promote the rapid outflow of QPs from the qubit junction and to prevent the inflow to the junction of QPs from remote parts of the qubit circuit. With these steps to mitigate the various forms of nonequilibrium QP poisoning, an SFQ gate error of order 0.1% is achievable using resonant SFQ pulse trains [23]. Ultimately, more complex control sequences involving nonuniform SFQ-pulse spacing should enable single-qubit gate error of order 0.01% [31,32], on par with that achieved using microwave-based gates but with a significant reduction in hardware footprint for the control system.

ACKNOWLEDGMENTS

We thank E. Leonard Jr. and M. A. Beck for stimulating discussions. C.H.L. was additionally funded by National Science Foundation (NSF) Award No. DMR-1747426. We thank M. Castellanos-Beltran and A. Sirois of National Institute of Standards and Technology (NIST) for assistance with SFQ-driver design, layout and testing. This research was sponsored in part by the Wisconsin Alumni Research Foundation (WARF) Accelerator. The SFQ-driver and fabrication work was partially supported by the Office of the Director of National Intelligence (ODNI), Intelligence Advanced Research Projects Activity (IARPA), under Interagency Agreement No. IARPA-20001-D2022-2203120004. Portions of this work were performed at the University of Wisconsin-Madison Wisconsin Centers for Nanoscale Technology, partially supported by the NSF through the University of Wisconsin Materials Research Science and Engineering Center (DMR-1720415). This work was performed in part under the auspices of the U.S. Department of Energy by the Lawrence Livermore National Laboratory under Contract No. DE-AC52-07NA27344. We gratefully acknowledge support from the NIST Program on Scalable Superconducting Computing and the National Nuclear Security Administration Advanced Simulation and Computing Beyond Moore's Law program (Grant No. LLNL-ABS-795437).

APPENDIX A: FABRICATION OF THE QUANTUM-CLASSICAL MCM

1. Qubit

The qubit chip is fabricated on a high-resistivity (> 10 kΩ-cm) 3-in. Si substrate with 100 crystal orientation. The native oxide of the silicon is stripped in dilute (2%) hydrofluoric acid for 60 s immediately prior to transfer of the wafer into the sputter deposition chamber used for growth of the 100-nm Nb base electrode. We use an i-line projection lithography tool to define the qubit islands and readout resonators. We then etch the Nb using BCl_3-Cl_2 chemistry in an inductively coupled plasma reactive-ion-etch tool. We use an electron-beam writer to define the Dolan bridges for the qubit junctions; the Al-AlO_x-Al junctions are then formed by double-angle evaporation and thermal oxidation in an electron-beam evaporator.

2. SFQ driver

The driver circuits are fabricated at the NIST Boulder Microfabrication Facility. The substrates used are 3-in. Si wafers with 150 nm of thermal oxide. The fabrication of the drivers is based on the process for SFQ digital circuits described in Ref. [65] with the following changes: (1) only three superconducting layers are used, requiring only one chemical-mechanical-planarization step before deposition of the second Nb layer; (2) the top Nb layer is used as the ground plane; (3) the barrier material used for the *S*-*I*-*S* junctions is amorphous Si and external shunt resistors are needed to bring the damping of these *S*-*I*-*S* junctions near the critical regime with Stewart-McCumber parameter $\beta_c \sim 2$; (4) the critical current density of the junctions is 1 kA/cm^2 and the characteristic junction frequency is 240 GHz; and (5) the shunt resistors are made of Pd-Au alloy films with a sheet resistance of 2 Ω/□, deposited by electron-beam evaporation and defined by a two-layer lift-off resist process.

3. MCM

The fabrication steps for the under-bump and In-bump layers deposited on each chip are similar to those described in Ref. [66] but with a target bump thickness of 5 μm. Additionally, hydrogen plasma cleaning before bonding is avoided to prevent potential contamination of Nb layers used both in the SFQ and qubit chips. The MCM is

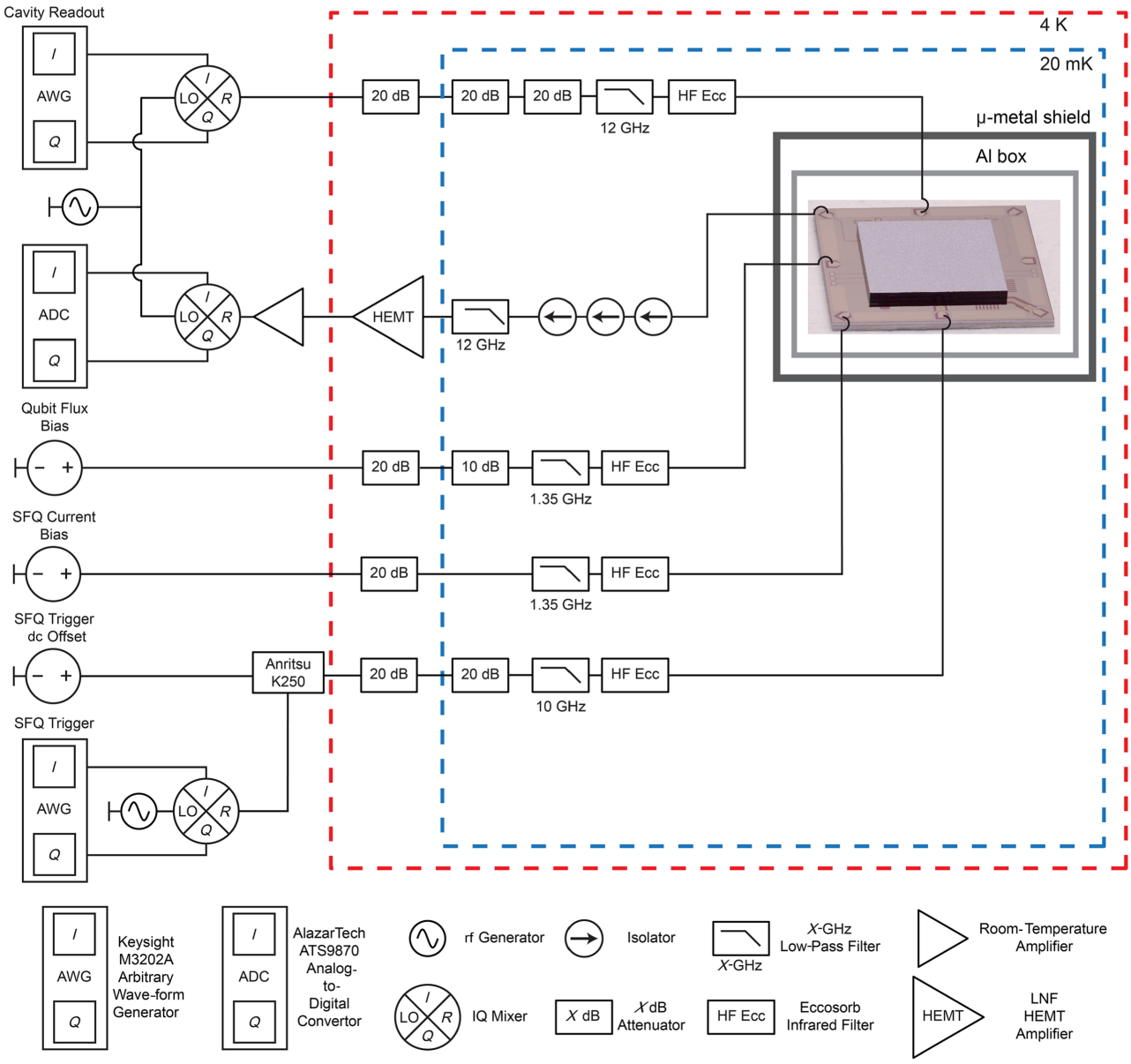

FIG. 9. The wiring diagram of the experiments.

bonded in a commercial flip-chip bonder. Before bonding, the components are aligned to $\pm$ 1.0 μm. The coplanarity is adjusted to be less than 100 μrad. The bonding force used is 21.6 kN, which, given optical profilometer measurements of the bump thickness (4.6 $\pm$ 0.2 μm) and top contact area (260 μm^2) for the 2193 bumps on each chip, results in a calculated effective pressure of 3.9×10^{10} N/m^2 and an expected resulting chip gap of 6.4 $\pm$ 0.3 μm.

APPENDIX B: WIRING

The experimental setup and wiring are shown in Fig. 9.

APPENDIX C: IMPACT OF SFQ-PULSE ERRORS

In addition to incoherent error from QP poisoning, the instability of the SFQ-pulse delivery represents another potential error channel. In Fig.2(a), we see that the Rabi frequency associated with resonant SFQ drive is not a constant over the full range of current bias; similar behavior has been seen in Refs. [27,30]. In Fig. 10(a), we plot the extracted Rabi frequency versus the bias current. We find relative variation in the Rabi frequency of order 5% over the bias current range considered. In the following, we examine the possibility that this variation is due to SFQ driver errors, namely, missed SFQ pulses or delivery of double pulses, and we estimate the resulting contribution to the SFQ gate error. For ideal operation of

the SFQ driver, one pulse is delivered to the qubit per clock cycle, where the clock cycle $1/f_{\mathrm{SFQ}}$ is set by the frequency f_{SFQ} of the microwave trigger pulse. Pulse dropouts will result in systematic underrotation of the qubit state and a reduction in the Rabi frequency, while double pulses will cause overrotation of the qubit and an increase in the Rabi frequency.

We define the SFQ-pulse probability P_{SFQ} in three regimes. For $P_{\mathrm{SFQ}} < 1$, one pulse is delivered per clock cycle with probability P_{SFQ}; the probability of a pulse dropout is $1 - P_{\mathrm{SFQ}}$. For $P_{\mathrm{SFQ}} = 1$, exactly one SFQ pulse is delivered per cycle of the trigger wave form. Finally, for $P_{\mathrm{SFQ}} > 1$, a double SFQ pulse is delivered with probability $P_{\mathrm{SFQ}} - 1$, while a single SFQ pulse is delivered with probability $2 - P_{\mathrm{SFQ}}$.

Following Ref. [23], we perform Monte Carlo simulations of the gate error and leakage to the $|2\rangle$ state for a $Y/2$ gate realized with the parameters of the SFQ driver-qubit pair used in these experiments; the simulation results are shown in Fig. 10(b). We find increased gate error and leakage as the probability of pulse dropouts or double pulses increases. For a pulse-dropout or double-pulse probability less than 3%, compatible with the variation in Rabi frequency over the bias current range from 40 μA to 120 μA, we put an upper bound on gate error of approximately 0.2%. While instability of the SFQ driver does not currently limit gate fidelity, it is possible that SFQ-pulse errors will be a dominant source of infidelity in SFQ gates once QP poisoning is fully suppressed.

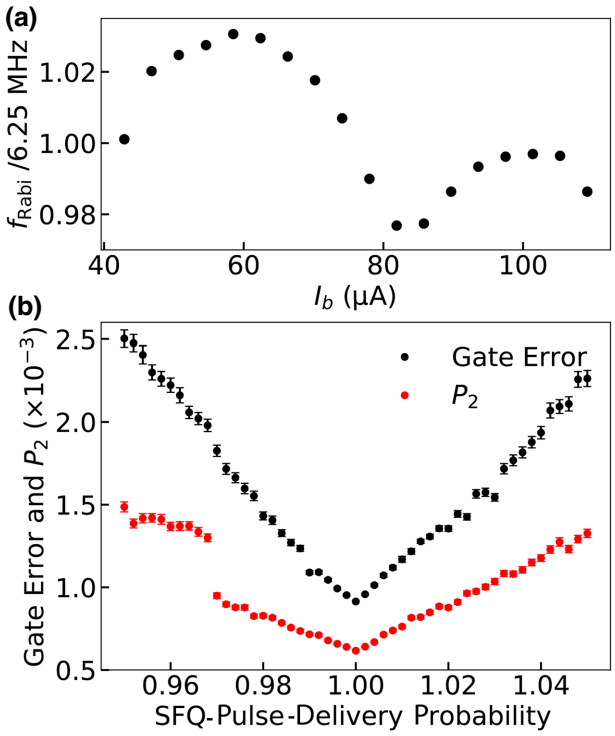

FIG. 10. The stability of the SFQ-pulse delivery and its effect on qubit control. (a) The scaled Rabi oscillation frequency f_{Rabi} extracted from Fig. 2(a) as a function of I_b. Over a bias current range from 40 to 120 μA, we find approximately ±3% variation in f_{Rabi} around the value 6.25 MHz. A possible explanation for the variation in Rabi frequency is that the number of SFQ pulses delivered per cycle of the trigger wave form is either less than or greater than one. (b) The simulated gate error and leakage to the $|2\rangle$ state for a $\pi/2$ gate implemented with an imperfect SFQ-pulse driver. The gate error and leakage both increase in the presence of SFQ-pulse dropouts and double pulses.

APPENDIX D: SFQ-QUBIT PARAMETERS

In Table I, we list the measured and extracted parameters of the SFQ-qubit pair used in these experiments.

APPENDIX E: GENERALIZED RABI SCAN WITH SFQ CONTROL

The number of lobes in the polar plot of Fig. 2(c) is twice of the ratio of the qubit frequency f_{01} to the SFQ drive frequency f_{SFQ}. In this paper, $f_{\mathrm{SFQ}} = f_{01}/4$, so we see $4 \times 2 = 8$ lobes in the plot. Four of these lobes are easy to understand: in the laboratory frame, the qubit state vector winds four times around the Bloch sphere in between SFQ pulses, so it samples each azimuthal angle 4 times per SFQ clock cycle. In addition, with the pulse sequence used here, it is impossible to distinguish positive and negative SFQ rotations R_{SFQ}, as the final $X/2$ gate maps the qubit state vector to locations on the Bloch sphere with the same polar angle (and with azimuthal angle differing by π). Thus, instead of four lobes, we find eight lobes.

TABLE I. The parameters of the devices used in the experiments. The resonator and qubit frequencies are measured by spectroscopy. The qubit baseline coherence times T_1 and $T_{2,\mathrm{white}}$ are extracted from microwave-based inversion-recovery and echo sequences. $T_{1,\mathrm{qp}}$ is extracted from nonlinear fits to the inversion recovery signals shown in Fig. 5. The SFQ operation parameters, including the trigger frequency, trigger power, trigger dc offset, and current bias, are chosen to maximize the SFQ-based qubit gate fidelity. The SFQ-qubit coupling capacitance is calculated following [23] from the measured Rabi frequency shown in Fig. 10(a).

Description	Symbol	Value
Readout-resonator frequency	f_{RO}	6.786 GHz
Qubit maximum operating frequency	f_{01}	4.906 GHz
Qubit energy relaxation time	T_1	26 μs
Qubit phase relaxation time	$T_{2,\mathrm{white}}$	20 μs
Qubit energy relaxation time per QP	$T_{1,\mathrm{qp}}$	6.8 μs
SFQ trigger frequency	$\omega_{\mathrm{SFQ}}/2\pi$	1.226 GHz
SFQ trigger power		−45 dBm
SFQ trigger dc offset		90 μA
SFQ current bias	I_b	80 μA
SFQ-qubit coupling capacitance	C_{SFQ}	180 aF

TABLE II. A list of the 24 composite single-qubit Clifford gates used in this work and their lengths in units of the $\pi/2$ gate length.

Gate length ($\pi/2$ gates)	Gate sequences		
0	I		
1	$\pm X/2$		
	$\pm Y/2$		
2	X		
	Y		
	$X/2$,	$\pm Y/2$	
	$-X/2$,	$\pm Y/2$	
	$Y/2$,	$\pm X/2$	
	$-Y/2$,	$\pm X/2$	
3	X,	$\pm Y/2$	
	Y,	$\pm X/2$	
	$-X/2$,	$\pm Y/2$,	$X/2$
	$\pm X/2$,	$Y/2$,	$\pm X/2$
4	X,	Y	

APPENDIX F: SINGLE-QUBIT CLIFFORD GATES

The 24 composite single-qubit Clifford gates are listed in Table II.

APPENDIX G: CHARACTERIZATION OF SFQ-BASED GATES WITH DRIVE AT $f_{01}/2$

We also use IRB to characterize SFQ-based control at the first subharmonic $f_{01}/2$ of the qubit fundamental frequency; the results are shown in Fig. 11. The average error per Clifford gate is 1.8(2)%, which is slightly higher than the result obtained at a drive frequency $f_{01}/4$. It is likely that the degraded fidelity at the higher drive frequency is due to the higher rate of photon-assisted QP generation associated with the shorter interpulse spacing.

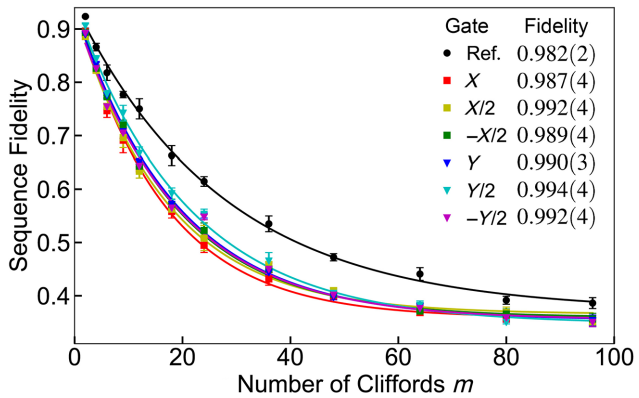

FIG. 11. The IRB of resonant SFQ-based gates implemented at drive frequency $f_{01}/2$.

APPENDIX H: MEASUREMENT OF SHORT-TIME RESPONSE OF THE QUBIT TO QUASIPARTICLE INJECTION

The 50-ns injection pulse and the fast 96-ns qubit readout are used to probe the short-time response of the qubit to quasiparticle injection by off-resonant SFQ pulses, as described in Fig. 6. The reduction in measurement integration time leads, of course, to reduced fidelity for the measurement; however, it is straightforward to compensate by increasing the number of averages. For each point in Fig. 6, we use a two-component Gaussian fit to the results of 5000 single-shot heterodyne measurements to extract the occupation of the qubit $|1\rangle$ state. We then repeat this experiment 300 (150) times for Q_1 (Q_2) and average the results of those trials to obtain the data presented in this paper. This short measurement interval is used only to acquire this data set, for which high timing resolution is required. For all other data presented in this paper, the measurement integration time is in the range 1–2 μs.

APPENDIX I: FREQUENCY-DOMAIN ANALYSIS OF SFQ PULSES

We consider an SFQ pulse with a Gaussian envelope in the time domain:

$$V_{\mathrm{SFQ}}(t) = \frac{\Phi_0}{\sqrt{2\pi}\sigma} e^{\frac{-t^2}{2\sigma^2}}, \tag{I1}$$

where Φ_0 is the magnetic flux quantum and σ is the standard deviation of the pulse in time. The Fourier transform

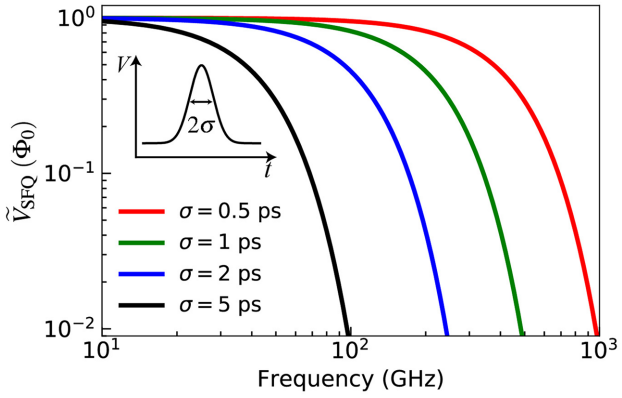

FIG. 12. The Fourier transform of the Gaussian SFQ pulses with varying standard deviation σ in the range 0.5–5 ps. In the Fourier-domain representation of the pulse, the standard deviation is $\sigma_f = (2\pi\sigma)^{-1}$. Narrower SFQ pulses in the time domain involve more spectral weight above the Al energy gap $2\Delta_{\mathrm{Al}}/h \sim 100$ GHz, where there is the possibility of photon-assisted QP generation.

of the SFQ pulse is given by

$$\widetilde{V}_{\mathrm{SFQ}}(f) = \Phi_0 e^{-\frac{f^2}{2\sigma_f^2}}, \tag{I2}$$

where $\sigma_f = (2\pi\sigma)^{-1}$ is the standard deviation of the pulse in the frequency domain. For typical Nb-based SFQ devices [16], σ is of the order of 1 ps. In Fig. 12, we plot $\widetilde{V}_{\mathrm{SFQ}}(f)$ for Gaussian SFQ pulses with four values of σ. For shorter pulses, the SFQ transient involves significant spectral weight at frequencies above the Al energy gap (approximately 100 GHz). Pair-breaking photons emitted by the transient can couple resonantly to the qubit structure via the spurious millimeter-wave antenna modes of the device. To suppress this form of QP poisoning, it is possible to intentionally broaden the SFQ pulses by increasing the damping of the SFQ driver. As the qubit oscillation period is 2 orders of magnitude larger than the SFQ-pulse width, broadening the SFQ pulse to, say, $\sigma = 5$ ps will have a negligible effect on the coherent qubit rotation induced by the SFQ pulse.

[1] R. Barends *et al.*, Superconducting quantum circuits at the surface code threshold for fault tolerance, Nature **508**, 500 (2014).

[2] T. Walter, P. Kurpiers, S. Gasparinetti, P. Magnard, A. Potočnik, Y. Salathé, M. Pechal, M. Mondal, M. Oppliger, C. Eichler, and A. Wallraff, Rapid High-Fidelity Single-Shot Dispersive Readout of Superconducting Qubits, Phys. Rev. Appl. **7**, 1 (2017).

[3] A. Opremcak, C.-H. Liu, C. Wilen, K. Okubo, B. G. Christensen, D. Sank, T. C. White, A. Vainsencher, M. Giustina, A. Megrant, B. Burkett, B. L. Plourde, and R. McDermott, High-Fidelity Measurement of a Superconducting Qubit Using an On-Chip Microwave Photon Counter, Phys. Rev. X **11**, 11027 (2021).

[4] A. G. Fowler, M. Mariantoni, J. Martinis, and A. N. Cleland, Surface codes: Towards practical large-scale quantum computation, Phys. Rev. A **86**, 032324 (2012).

[5] F. Arute *et al.*, Quantum supremacy using a programmable superconducting processor, Nature **574**, 505 (2019).

[6] Y. Zhao *et al.*, Realization of an Error-Correcting Surface Code with Superconducting Qubits, Phys. Rev. Lett. **129**, 30501 (2021).

[7] S. Krinner, N. Lacroix, A. Remm, A. Di Paolo, E. Genois, C. Leroux, C. Hellings, S. Lazar, F. Swiadek, J. Herrmann, G. J. Norris, C. K. Andersen, M. Müller, A. Blais, C. Eichler, and A. Wallraff, Realizing repeated quantum error correction in a distance-three surface code, Nature **605**, 669 (2022).

[8] R. Acharya *et al.*, Suppressing quantum errors by scaling a surface code logical qubit, arXiv:2207.06431 (2022).

[9] S. Krinner, S. Storz, P. Kurpiers, P. Magnard, J. Heinsoo, R. Keller, J. Lütolf, C. Eichler, and A. Wallraff, Engineering cryogenic setups for 100-qubit scale superconducting circuit systems, EPJ Quantum Technol. **6**, 2 (2019).

[10] P. Magnard, S. Storz, P. Kurpiers, J. Schar, F. Marxer, J. Lütolf, T. Walter, J. C. Besse, M. Gabureac, K. Reuer, A. Akin, B. Royer, A. Blais, and A. Wallraff, Microwave Quantum Link between Superconducting Circuits Housed in Spatially Separated Cryogenic Systems, Phys. Rev. Lett. **125**, 260502 (2020).

[11] L. Stefanazzi, K. Treptow, N. Wilcer, C. Stoughton, C. Bradford, S. Uemura, S. Zorzetti, S. Montella, G. Cancelo, S. Sussman, A. Houck, S. Saxena, H. Arnaldi, A. Agrawal, H. Zhang, C. Ding, and D. I. Schuster, The QICK (Quantum Instrumentation Control Kit): Readout and control for qubits and detectors, Rev. Sci. Instrum. **93**, 044709 (2022).

[12] J. C. Bardin *et al.*, Design and characterization of a 28-nm bulk-CMOS cryogenic quantum controller dissipating less than 2 mW at 3 K, IEEE J. Solid-State Circuits **54**, 3043 (2019).

[13] J. P. G. Van DIjk *et al.*, A scalable cryo-CMOS controller for the wideband frequency-multiplexed control of spin qubits and transmons, IEEE J. Solid-State Circuits **55**, 2930 (2020).

[14] F. Lecocq, F. Quinlan, K. Cicak, J. Aumentado, S. A. Diddams, and J. D. Teufel, Control and readout of a superconducting qubit using a photonic link, Nature **591**, 575 (2021).

[15] J. P. Smith, B. A. Mazin, A. B. Walter, M. Daal, J. I. Bailey, C. Bockstiegel, N. Zobrist, N. Swimmer, S. Steiger, and N. Fruitwala, Flexible coaxial ribbon cable for high-density superconducting microwave device arrays, IEEE Trans. Appl. Supercond. **31**, 3 (2021).

[16] K. K. Likharev and V. K. Semenov, RSFQ Logic/memory family: A new Josephson-junction technology for sub-terahertz-clock-frequency digital systems, IEEE Trans. Appl. Supercond. **1**, 3 (1991).

[17] O. A. Mukhanov, Energy-efficient single flux quantum technology, IEEE Trans. Appl. Supercond. **21**, 760 (2011).

[18] I. I. Soloviev, N. V. Klenov, S. V. Bakurskiy, M. Y. Kupriyanov, A. L. Gudkov, and A. S. Sidorenko, Beyond Moore's technologies: Operation principles of a superconductor alternative, Beilstein J. Nanotechnol. **8**, 2689 (2017).

[19] Y. Okuma, N. Takeuchi, Y. Yamanashi, and N. Yoshikawa, Design and demonstration of an adiabatic-quantum-flux-parametron field-programmable gate array using Josephson-CMOS hybrid memories, IEEE Trans. Appl. Supercond **29**, 8 (2019).

[20] W. Wustmann and K. D. Osborn, Reversible fluxon logic: Topological particles allow ballistic gates along one-dimensional paths, Phys. Rev. B **101**, 1 (2020).

[21] K. D. Osborn and W. Wustmann, Reversible fluxon logic with optimized CNOT gate components, IEEE Trans. Appl. Supercond. **31**, 2 (2021).

[22] N. Takeuchi, T. Yamae, S. Member, and C. L. Ayala, Adiabatic quantum-flux-parametron: A tutorial review, IEICE Trans. Electron. **E105-C**, 251 (2022).

[23] R. McDermott and M. G. Vavilov, Accurate Qubit Control with Single Flux Quantum Pulses, Phys. Rev. Appl. **2**, 1 (2014).

[24] A. Opremcak, I. V. Pechenezhskiy, C. Howington, B. G. Christensen, M. A. Beck, E. Leonard, J. Suttle, C. Wilen, K. N. Nesterov, G. J. Ribeill, T. Thorbeck, F. Schlenker, M. G. Vavilov, B. L. Plourde, and R. McDermott, Measurement of a superconducting qubit with a microwave photon counter, Science **1242**, 1239 (2018).

[25] C. Howington, A. Opremcak, R. McDermott, A. Kirichenko, O. A. Mukhanov, and B. L. Plourde, Interfacing superconducting qubits with cryogenic logic: Readout, IEEE Trans. Appl. Supercond. **29**, 5 (2019).

[26] R. McDermott, M. G. Vavilov, B. L. Plourde, F. K. Wilhelm, P. J. Liebermann, O. A. Mukhanov, and T. A. Ohki, Quantum-classical interface based on single flux quantum digital logic, Quantum Sci. Technol. **3**, 1 (2018).

[27] E. Leonard, M. A. Beck, J. Nelson, B. G. Christensen, T. Thorbeck, C. Howington, A. Opremcak, I. V. Pechenezhskiy, K. Dodge, N. P. Dupuis, M. D. Hutchings, J. Ku, F. Schlenker, J. Suttle, C. Wilen, S. Zhu, M. G. Vavilov, B. L. Plourde, and R. McDermott, Digital Coherent Control of a Superconducting Qubit, Phys. Rev. Appl. **11**, 1 (2019).

[28] L. I. Glazman and G. Catelani, Bogoliubov quasiparticles in superconducting qubits, SciPost Phys. Lect. Notes **31**, 1 (2021).

[29] A. J. Sirois, M. Castellanos-Beltran, A. E. Fox, S. P. Benz, and P. F. Hopkins, Josephson microwave sources applied to quantum information systems, IEEE Trans. Quantum Eng. **1**, 1 (2021).

[30] L. Howe, M. Castellanos-Beltran, A. J. Sirois, D. Olaya, J. Biesecker, P. D. Dresselhaus, S. P. Benz, and P. F. Hopkins, Digital Control of a Superconducting Qubit Using a Josephson Pulse Generator at 3 K, PRX Quantum **3**, 1 (2022).

[31] P. J. Liebermann and F. K. Wilhelm, Optimal Qubit Control Using Single-Flux Quantum Pulses, Phys. Rev. Appl. **6**, 2 (2016).

[32] K. Li, R. McDermott, and M. G. Vavilov, Hardware-Efficient Qubit Control with Single-Flux-Quantum Pulse Sequences, Phys. Rev. Appl. **12**, 1 (2019).

[33] M. R. Jokar, R. Rines, and F. T. Chong, Practical implications of SFQ-based two-qubit gates, Proceedings—2021 IEEE International Conference on Quantum Computing and Engineering, QCE 2021, 402 (2021).

[34] M. R. Jokar, R. Rines, G. Pasandi, H. Cong, A. Holmes, Y. Shi, M. Pedram, and F. T. Chong, DigiQ: A scalable digital controller for quantum computers using SFQ logic, 2022 IEEE International Symposium on High-Performance Computer Architecture (HPCA) 2022 **1**, 400 (2022).

[35] R. P. Riwar and G. Catelani, Efficient quasiparticle traps with low dissipation through gap engineering, Phys. Rev. B **100**, 144514 (2019).

[36] D. Gottesman, A theory of fault-tolerant quantum computation, Phys. Rev. A **57**, 30 (1997).

[37] E. Knill, D. Leibfried, R. Reichle, J. Britton, R. B. Blakestad, J. D. Jost, C. Langer, R. Ozeri, S. Seidelin, and D. J. Wineland, Randomized benchmarking of quantum gates, Phys. Rev. A—At., Mol., Opt. Phys. **77**, 1 (2008).

[38] J. M. Chow, L. Dicarlo, J. M. Gambetta, F. Motzoi, L. Frunzio, S. M. Girvin, and R. J. Schoelkopf, Optimized driving of superconducting artificial atoms for improved single-qubit gates, Phys. Rev. A—At., Mol., Opt. Phys. **82**, 2 (2010).

[39] J. Kelly *et al.*, Optimal Quantum Control Using Randomized Benchmarking, Phys. Rev. Lett. **112**, 1 (2014).

[40] E. Magesan, J. M. Gambetta, B. R. Johnson, C. A. Ryan, J. M. Chow, S. T. Merkel, M. P. Da Silva, G. A. Keefe, M. B. Rothwell, T. A. Ohki, M. B. Ketchen, and M. Steffen, Efficient Measurement of Quantum Gate Error by Interleaved Randomized Benchmarking, Phys. Rev. Lett. **109**, 1 (2012).

[41] J. Wallman, C. Granade, R. Harper, and S. T. Flammia, Estimating the coherence of noise, New J. Phys. **17**, 113020 (2015).

[42] P. J. O'Malley *et al.*, Qubit Metrology of Ultralow Phase Noise Using Randomized Benchmarking, Phys. Rev. Appl. **3**, 1 (2015).

[43] Z. Chen, Ph.D. thesis, Department of Physics, UC Santa Barbara, 2018.

[44] G. Catelani, S. E. Nigg, S. M. Girvin, R. J. Schoelkopf, and L. I. Glazman, Decoherence of superconducting qubits caused by quasiparticle tunneling, Phys. Rev. B—Condens. Matter Mater. Phys. **86**, 1 (2012).

[45] K. Serniak, M. Hays, G. De Lange, S. Diamond, S. Shankar, L. D. Burkhart, L. Frunzio, M. Houzet, and M. H. Devoret, Hot Nonequilibrium Quasiparticles in Transmon Qubits, Phys. Rev. Lett. **121**, 157701 (2018).

[46] L. Grünhaupt, N. Maleeva, S. T. Skacel, M. Calvo, F. Levy-Bertrand, A. V. Ustinov, H. Rotzinger, A. Monfardini, G. Catelani, and I. M. Pop, Loss Mechanisms and Quasiparticle Dynamics in Superconducting Microwave Resonators Made of Thin-Film Granular Aluminum, Phys. Rev. Lett. **121**, 117001 (2018).

[47] C. Wilen, S. Abdullah, N. A. Kurinsky, C. Stanford, L. Cardani, G. D'Imperio, C. Tomei, L. Faoro, L. B. Ioffe, C. H. Liu, A. Opremcak, B. G. Christensen, J. L. DuBois, and R. McDermott, Correlated charge noise and relaxation errors in superconducting qubits, Nature **594**, 369 (2021).

[48] I. Siddiqi, Engineering high-coherence superconducting qubits, Nat. Rev. Mater. **6**, 875 (2021).

[49] I. M. Pop, K. Geerlings, G. Catelani, R. J. Schoelkopf, L. I. Glazman, and M. H. Devoret, Coherent suppression of electromagnetic dissipation due to superconducting quasiparticles, Nature **508**, 369 (2014).

[50] S. Gustavsson, F. Yan, G. Catelani, J. Bylander, A. Kamal, J. Birenbaum, D. Hover, D. Rosenberg, G. Samach, A. P. Sears, S. J. Weber, J. L. Yoder, J. Clarke, A. J. Kerman, F. Yoshihara, Y. Nakamura, T. P. Orlando, and W. D. Oliver, Suppressing relaxation in superconducting qubits by quasiparticle pumping, Science **354**, 1573 (2016).

[51] C. Wang, Y. Y. Gao, I. M. Pop, U. Vool, C. Axline, T. Brecht, R. W. Heeres, L. Frunzio, M. H. Devoret, G. Catelani, L. I. Glazman, and R. J. Schoelkopf, Measurement and control of quasiparticle dynamics in a superconducting qubit, Nat. Commun. **5**, 1 (2014).

[52] A. P. Vepsäläinen, A. H. Karamlou, J. L. Orrell, A. S. Dogra, B. Loer, F. Vasconcelos, D. K. Kim, A. J. Melville, B. M. Niedzielski, J. L. Yoder, S. Gustavsson, J. A. Formaggio, B. A. VanDevender, and W. D. Oliver, Impact of ionizing radiation on superconducting qubit coherence, Nature **584**, 551 (2020).

[53] U. Patel, I. V. Pechenezhskiy, B. L. Plourde, M. G. Vavilov, and R. McDermott, Phonon-mediated quasiparticle poisoning of superconducting microwave resonators, Phys. Rev. B. **96**, 1 (2017).

[54] O. Rafferty, S. Patel, C. H. Liu, S. Abdullah, C. Wilen, D. C. Harrison, and R. McDermott, Spurious antenna modes of the transmon qubit, arXiv:2103.06803 (2021).

[55] C. H. Liu, D. C. Harrison, S. Patel, C. Wilen, O. Rafferty, A. Shearrow, A. Ballard, V. Iaia, J. Ku, B. L. T. Plourde, and R. McDermott, Quasiparticle poisoning of superconducting qubits from resonant absorption of pair-breaking photons, arXiv:2203.06577 (2022).

[56] V. Iaia, J. Ku, A. Ballard, C. P. Larson, E. Yelton, C. H. Liu, S. Patel, R. McDermott, and B. L. Plourde, Phonon down-conversion to suppress correlated errors in superconducting qubits, Nat. Commun. **13**, 1 (2022).

[57] M. Houzet, K. Serniak, G. Catelani, M. H. Devoret, and L. I. Glazman, Photon-Assisted Charge-Parity Jumps in a Superconducting Qubit, Phys. Rev. Lett. **123**, 107704 (2019).

[58] X. Pan, H. Yuan, Y. Zhou, L. Zhang, J. Li, S. Liu, Z. H. Jiang, G. Catelani, L. Hu, and F. Yan, Engineering superconducting qubits to reduce quasiparticles and charge noise, Nat. Commun. **13:7196**, 7196 (2022).

[59] S. Diamond, V. Fatemi, M. Hays, H. Nho, P. D. Kurilovich, T. Connolly, V. R. Joshi, K. Serniak, L. Frunzio, L. I. Glazman, and M. H. Devoret, Distinguishing Parity-Switching Mechanisms in a Superconducting Qubit, PRX Quantum **3**, 040304 (2022).

[60] WRspice is part of the free open-source XicTools software package for integrated circuit design from Whiteley Research Inc., available at http://wrcad.com.

[61] K. Kalashnikov, W. T. Hsieh, W. Zhang, W.-S. Lu, P. Kamenov, A. Di Paolo, A. Blais, M. E. Gershenson, and M. Bell, Bifluxon: Fluxon-Parity-Protected Superconducting Qubit, PRX Quantum **1**, 1 (2020).

[62] J. Martinis, Saving superconducting quantum processors from decay and correlated errors generated by gamma and cosmic rays, Npj Quantum Inf. **7**, 90 (2021).

[63] A. Bargerbos, L. J. Splitthoff, M. Pita-Vidal, J. J. Wesdorp, Y. Liu, P. Krogstrup, L. P. Kouwenhoven, C. K. Andersen, and L. Grünhaupt, Mitigation of quasiparticle loss in superconducting qubits by phonon scattering, arXiv:2207.12754 (2022).

[64] G. Catelani and J. P. Pekola, Using materials for quasiparticle engineering, Mater. Quantum Technol. **2**, 013001 (2022).

[65] D. Olaya, M. Castellanos-Beltran, J. Pulecio, J. Biesecker, S. Khadem, T. Lewitt, P. Hopkins, P. Dresselhaus, and S. Benz, Planarized process for single-flux-quantum circuits with self-shunted Nb/Nb_xSi_{1-x}/Nb Josephson junctions, IEEE Trans. Appl. Supercond. **29**, 1 (2019).

[66] T. J. Lucas, J. P. Biesecker, W. B. Doriese, S. M. Duff, G. C. Hilton, J. N. Ullom, M. R. Vissers, and D. R. Schmidt, Indium bump process for low-temperature detectors and readout, J. Low Temp. Phys. **209**, 1 (2022).